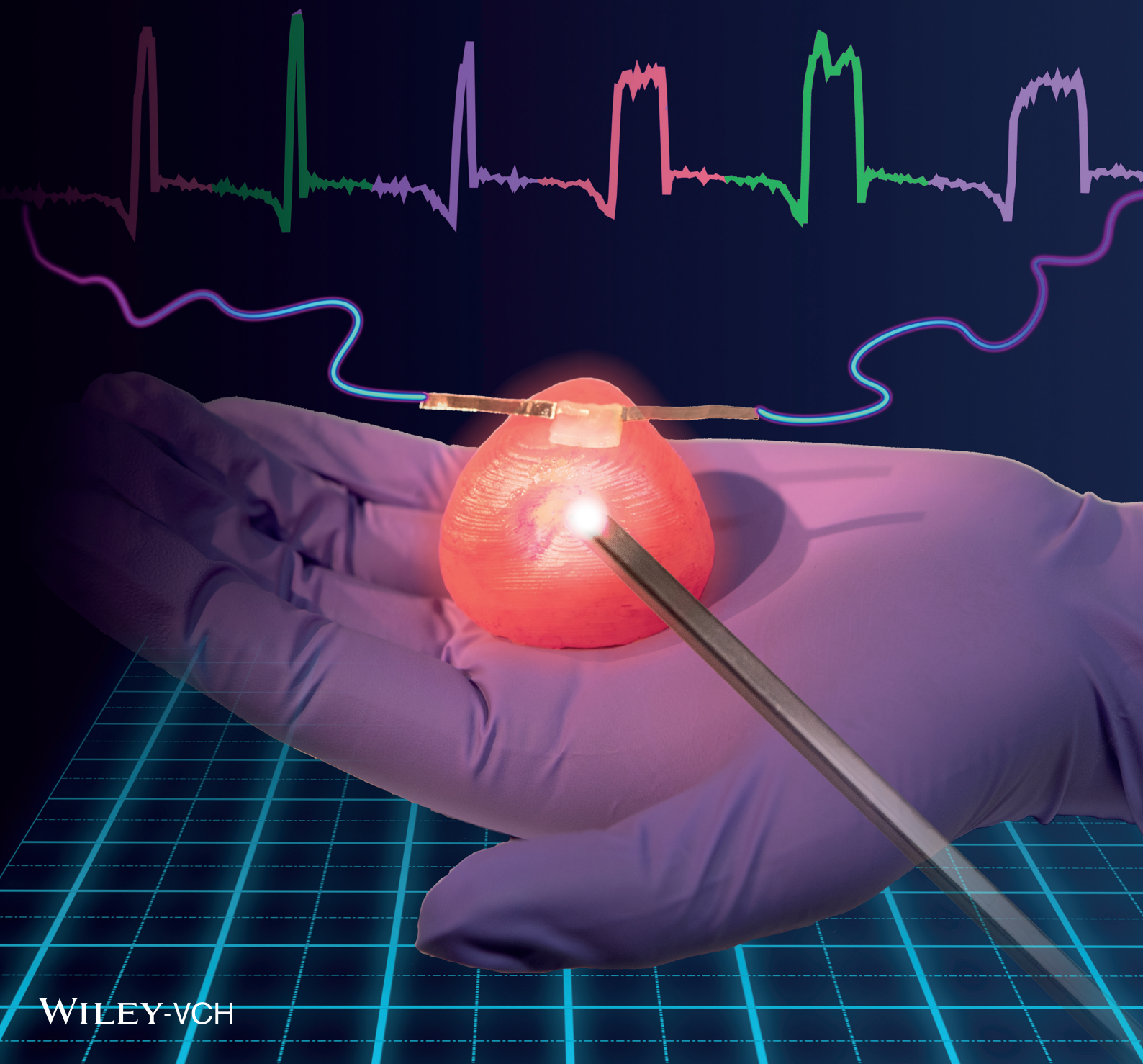


Vol. 3 • No. 3 • March • 2018

www.advmattechnol.com

ADVANCED MATERIALS TECHNOLOGIES



WILEY-VCH

3D Printed Organ Models with Physical Properties of Tissue and Integrated Sensors

Kaiyan Qiu, Zichen Zhao, Ghazaleh Haghiashtiani, Shuang-Zhuang Guo, Mingyu He, Ruitao Su, Zhijie Zhu, Didarul B. Bhuiyan, Paari Murugan, Fanben Meng, Sung Hyun Park, Chih-Chang Chu, Brenda M. Ogle, Daniel A. Saltzman, Badrinath R. Konety, Robert M. Sweet,* and Michael C. McAlpine*

The design and development of novel methodologies and customized materials to fabricate patient-specific 3D printed organ models with integrated sensing capabilities can yield advances in smart surgical aids for preoperative planning and rehearsal. Here, 3D printed prostate models are demonstrated with physical properties of tissue and integrated soft electronic sensors using custom-formulated polymeric inks. The models show high quantitative fidelity in static and dynamic mechanical properties, optical characteristics, and anatomical geometries to patient tissues and organs. The models offer tissue-mimicking tactile sensation and behavior and thus can be used for the prediction of organ physical behavior under deformation. The prediction results show good agreement with values obtained from simulations. The models also allow the application of surgical and diagnostic tools to their surface and inner channels. Finally, via the conformal integration of 3D printed soft electronic sensors, pressure applied to the models with surgical tools can be quantitatively measured.

States alone.^[2] Although the complete elimination of errors in clinical procedures is impossible, effective preoperative planning and rehearsal could play a vital role in decreasing their occurrence. Medical professionals often rely on magnetic resonance imaging (MRI), computed tomography, and/or 3D virtual visualization to develop an understanding of the unique anatomies and disease states of patient organs.^[3,4] However, these approaches often fail to provide information regarding the intricate orientations, dimensions, and kinesthetic feedback within the organs.^[3,4] Physical organ models offer an effective option for representing the 3D structure of the organs. Yet, molded organ models can lack patient-specificity and exhibit inaccurate or poorly adjustable physical properties.^[5,6]

One recent study suggests that medical errors are the third leading cause of death in the United States, resulting in a mean death rate of 251 454 patients annually.^[1] In addition, over 4000 surgical “never event” claims occur each year in the United

States alone.^[2] Although the complete elimination of errors in clinical procedures is impossible, effective preoperative planning and rehearsal could play a vital role in decreasing their occurrence. Medical professionals often rely on magnetic resonance imaging (MRI), computed tomography, and/or 3D virtual visualization to develop an understanding of the unique anatomies and disease states of patient organs.^[3,4] However, these approaches often fail to provide information regarding the intricate orientations, dimensions, and kinesthetic feedback within the organs.^[3,4] Physical organ models offer an effective option for representing the 3D structure of the organs. Yet, molded organ models can lack patient-specificity and exhibit inaccurate or poorly adjustable physical properties.^[5,6]

Recently, patient-specific 3D printed organ models have been introduced as tools for providing accurate anatomical details of the patient organs for preoperative planning, foreseeing intraoperative complications, and reducing the operation time for improving patient safety and

Dr. K. Qiu, G. Haghiashtiani, Dr. S.-Z. Guo, R. Su, Z. Zhu,
Dr. F. Meng, Dr. S. H. Park, Prof. M. C. McAlpine
Department of Mechanical Engineering
University of Minnesota
Minneapolis, MN 55455, USA
E-mail: mcalpine@umn.edu

Dr. Z. Zhao, Prof. R. M. Sweet
WWAMI Institute for Simulation in Healthcare
University of Washington
Seattle, WA 98195, USA
E-mail: rsweet@uw.edu

Dr. Z. Zhao, Prof. B. R. Konety, Prof. R. M. Sweet
Department of Urology
University of Minnesota
Minneapolis, MN 55455, USA

Dr. M. He, Prof. C.-C. Chu
Fiber Science and Biomedical Engineering Programs
Cornell University
Ithaca, NY 14853, USA

Dr. D. B. Bhuiyan, Prof. B. M. Ogle
Department of Biomedical Engineering
University of Minnesota
Minneapolis, MN 55455, USA

Prof. P. Murugan
Department of Laboratory Medicine and Pathology
University of Minnesota
Minneapolis, MN 55455, USA

Prof. D. A. Saltzman
Department of Surgery
University of Minnesota
Minneapolis, MN 55455, USA

 The ORCID identification number(s) for the author(s) of this article can be found under <https://doi.org/10.1002/admt.201700235>.

DOI: 10.1002/admt.201700235

surgical outcomes.^[7–13] However, the application of 3D printed organ models as advanced surgical aids is currently hampered in two main aspects. First, current 3D printed organ models, while anatomically correct, lack precise mimicry of the physical properties of real tissue.^[7] This limits their application for accurate prediction and replication of organ physical behavior, such as deformation and reaction force during surgical handling. The organ models are typically printed using commercial hard plastics and rubber-like materials (Polylactic acid, Polystyrene, NinjaFlex, etc.).^[14] There are significant differences in tactile sensation, mechanical properties, and color of these materials compared to their biological counterparts, limiting their effectiveness in preoperative planning, rehearsal with surgical tools, and other surgical tasks such as pressing and cutting.^[7,8] Ideally, a 3D printed organ model would match the mechanical and physical properties of the organ and tissue, including viscoelasticity and hardness. Second, current organ models lack the ability to collect quantitative feedback from organ and tissue handling. This important metric is an indicator of surgical performance and can provide important feedback for physical trainers or simulators. This feedback includes providing medical professionals with the ability to quantify and control the force ranges they apply to the organ during preoperative rehearsal and training.

Here we demonstrate a new concept in the development of 3D printed patient-specific prostate models using customized

polymeric inks to address the abovementioned issues. The developed model has physical properties closely matching those of prostate tissue and integrated sensing capabilities that can be used for advanced surgical aid applications. We chose the prostate as a proof-of-principle organ model, due to its relatively simple geometry. In addition, prostate surgeries have inherent risks for damaging the urethral sphincter and neurovascular bundle during prostate removal, and therefore, proper preoperative planning and rehearsal via a 3D printed prostate model may have implications for surgical outcomes in thousands of patients worldwide.^[15]

Figure 1a provides an overview of the concept: a patient-specific, 3D printed prostate model that exhibits the physical properties of tissue with high fidelity and provides sensing capabilities via integrated soft tactile sensors. Two potential surgical aid examples of the proposed model are also depicted in Figure 1a: organ physical behavior prediction and quantitative surgical rehearsal. The following six steps were conducted for the development and application of the advanced 3D printed prostate models: (1) collection and analysis of organ anatomy and properties of prostate tissue, including static and dynamic mechanical properties, hardness, and optical reflection (Figure 1b); (2) design and development of customized polymeric inks based on the tissue data, and ink fidelity analysis with the physical properties of tissue; (3) 3D printing of prostate models and anatomical fidelity analysis; (4) investigating

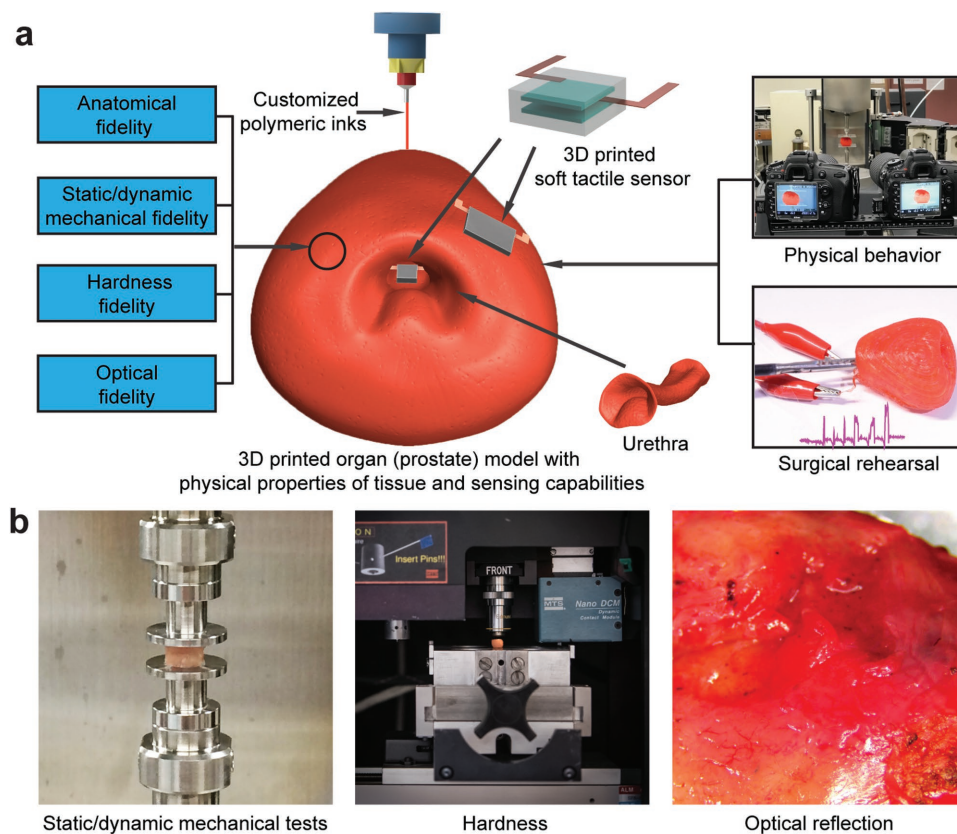


Figure 1. 3D printed patient-specific prostate model with physical properties of tissue and integrated sensing capabilities for advanced surgical rehearsal. a) Schematic of the 3D printed prostate model highlighting the various components, properties, and applications. b) Mechanical and optical tests for obtaining the physical and optical properties of patient prostate tissue samples to guide ink development.

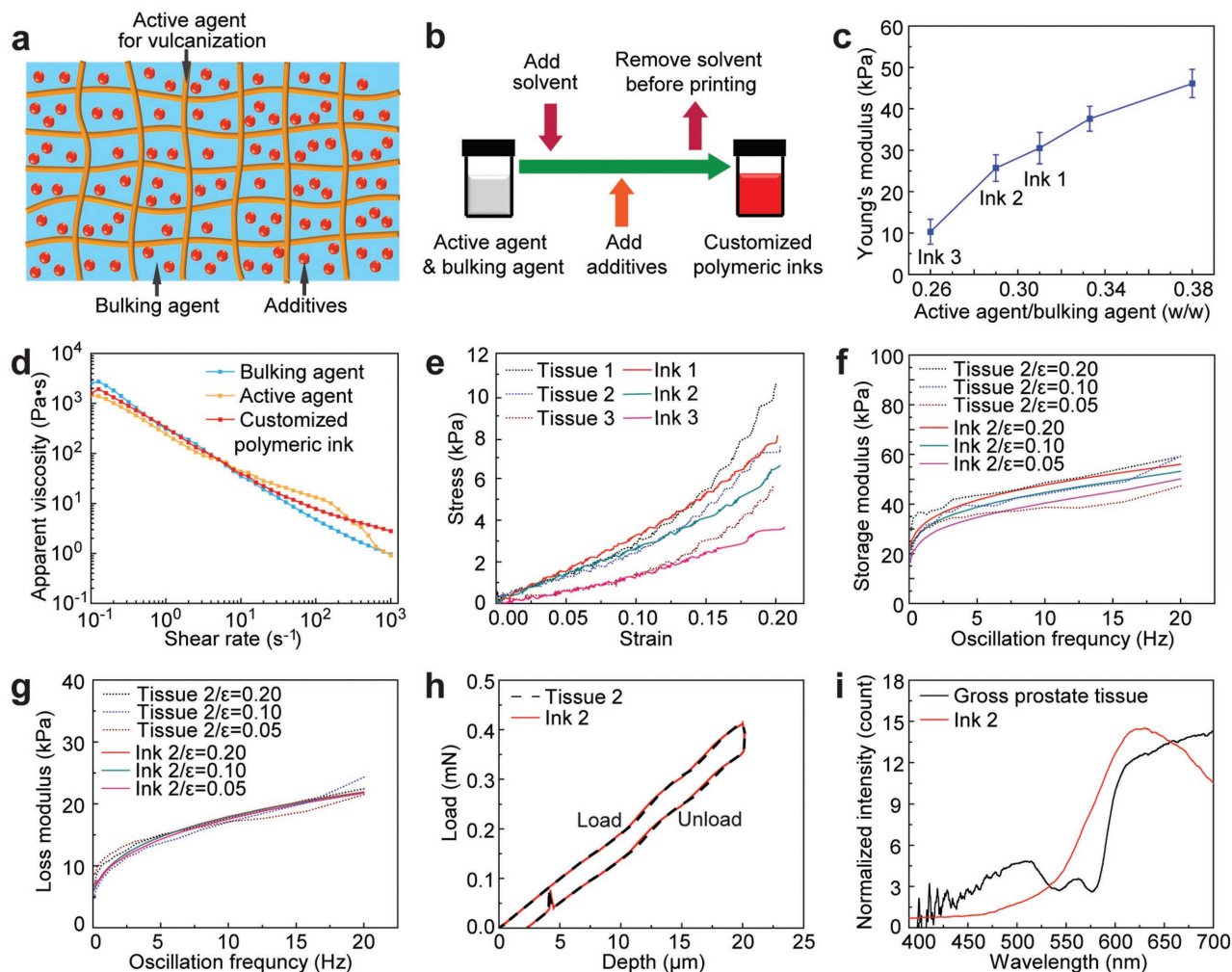


Figure 2. Design and development of customized polymeric inks based on patient-specific prostate tissue data, and resulting ink fidelity with physical properties of the tissue. a) Schematic of the composite structure of the customized polymeric inks. b) Preparation procedure for the customized polymeric inks. c) A plot of prime component weight ratios versus Young's moduli for the polymeric inks. d) Log-log plots of apparent viscosity versus shear rate for a customized polymeric ink (including its constituent components) used for printing the prostate model. e) Static compression fidelity via stress-strain curves between different patient prostate tissue samples (Tissues 1–3) and printed samples of customized polymeric inks (Inks 1–3). f) Dynamic compression fidelity of storage modulus between a patient prostate tissue sample (Tissue 2) and a sample of customized polymeric ink (Ink 2) at frequencies of 0.1–20 Hz and strains of 0.05, 0.10, and 0.20. g) Dynamic compression fidelity of loss modulus between a patient prostate tissue (Tissue 2) and a sample of customized polymeric ink (Ink 2) at frequencies of 0.1–20 Hz and strains of 0.05, 0.10, and 0.20. h) Hardness fidelity via load-depth curves between a patient prostate tissue sample (Tissue 2) and a sample of customized polymeric ink (Ink 2). i) Optical fidelity via reflection curves between patient prostate gross tissue and a customized polymeric ink (Ink 2).

the application of 3D printed prostate models as advanced surgical aids for quantitative prediction of organ physical behavior and comparison with corresponding finite element method (FEM) simulations; (5) 3D printing soft tactile sensors for integration on the model surfaces and interiors; (6) investigating the practical and quantitative aspects of the 3D printed prostate models as advanced surgical aids via the application of diagnostic and surgical tools.

A critical step is to formulate customized polymeric 3D printing inks to adequately mimic patient prostate tissue. There are several requirements for an ideal ink formulation, including adjustable properties, good printability, maintaining stable structures and properties during and after printing, vulcanization at room temperature within a

short time period, and convenient preparation. In general, the customized inks consisted of three main components: an active agent for vulcanization, a bulking agent, and additives (Figure 2a). The composite nature of the inks is analogous to human tissue.^[16,17] We ultimately selected silicone sealant (room temperature vulcanization) as the active agent to stabilize the structures, silicone grease as a bulking agent to contribute softness and flexibility, and additives for fine-tuning of color and/or printability. The prime components in the ink system are all silicone-based materials, which enables their homogeneous mixture. Silicone-based materials exhibit appropriate shear thinning behavior, resist polymer creep before crosslinking, and have good elasticity after crosslinking.

By adjusting the component ratios as a general preparative procedure for different ink formulations (Figure 2b,c and Figure S1 and Table S1, Supporting Information), the printability can be optimized and the properties of the inks can be tuned to match the different tissue mechanical properties. As shown in Figure 2c and Table S1 in the Supporting Information, by increasing the weight ratios of the active agent to the bulking agent (from 0.26 (0.82/3.18) to 0.38 (1.10/2.90)), the corresponding values of Young's moduli increase (from 10.3 ± 3.0 to 46.1 ± 3.4 kPa). This trend correlates with the increase of the crosslinking density, which can be used to tailor the mechanical properties of the inks. Thus, this trend can be utilized as a reference for adjusting the composition of the polymeric inks to match the tissue mechanical properties. Rheological properties of the two main components of the custom inks were used as a reference for adjusting the printing conditions (Figure 2d). As the shear rate increased from 10^{-1} to 10^3 s $^{-1}$, the apparent viscosity of the inks decreased from 10^3 to 10 Pa s or less, which confirms the shear thinning behavior of the developed inks. This facilitates the flow of the inks through fine nozzles during the 3D printing process.^[18]

Following development, a quantitative analysis of the inks allowed us to quantify the fidelity of the physical properties to tissue, including a comparison of static and dynamic compression, hardness, and optical reflection characteristics between the printed inks and their corresponding tissue samples. For quantitative analysis of fidelity of static compression, stress-strain curves for cylindrical samples from patient prostate tissue were compared to printed samples of customized polymeric inks (Figure 2e). At 0–0.15 strain range (an acceptable range for most surgical tasks on prostate), the customized polymeric inks 1, 2, and 3, containing different ratios of active and bulking agents (Table S1, Supporting Information), closely matched the general trends of stress-strain curves obtained from three prostate tissue samples, suggesting patient-specificity in ink composition. The Young's moduli for strains less than 10% for representative samples of inks 1 (31.6 kPa), 2 (26.0 kPa), and 3 (12.4 kPa) (see Figure 2c and Table S1, Supporting Information, for prime component ratios in the formulations, average modulus values, and corresponding standard deviations) are analogous to tissue samples 1 (25.7 kPa), 2 (20.3 kPa), and 3 (10.9 kPa). At high strains, the modulus values increase with a nonlinear trend for tissue samples (due to viscoelastic, poroelastic, and anisotropic properties of soft tissue)^[19–21] and polymeric ink samples (due to viscoelastic behavior). The values obtained for Young's moduli are also comparable to previous reports for the prostate tissue samples^[22] and are well below the values for typical 3D printed hard plastics and rubber-like materials. Indeed, the Young's moduli for commercial Loctite RTV silicone (595 CL, Young's modulus = 0.24 MPa) and NinjaFlex (Young's modulus = 15.20 MPa) are at least one order of magnitude higher than patient prostate tissue and our customized polymeric inks (Figure S2, Supporting Information).

After demonstrating the capability of tailoring ink composition to match the properties of a specific tissue, we chose the ink 2/tissue 2 pair as a representative example for the remainder of the characterization, 3D printing and proof of concept demonstrations. For quantitative analysis of the fidelity of dynamic compression properties, the mechanical responses

of cylindrical samples under applied dynamic compression were evaluated and compared for ink 2 and the corresponding tissue 2 (Figure 2f,g). Both storage (E') and loss (E'') moduli for cylindrical samples of tissue 2 and ink 2 at 0.05, 0.10, and 0.20 strains showed high fidelity. For the storage modulus, the values for both tissue and ink increased with increasing oscillation frequency (0.1–20 Hz) and strain (0.05–0.20). The trends of the obtained results are similar to previous reports for biological tissue (for example, human cervix tissue) exhibiting viscoelastic properties.^[21] For the loss modulus, the values only indicate a clear increase with oscillation frequency.

For quantitative analysis of the fidelity of hardness, a nanoindentation methodology was applied.^[23,24] The hardness properties of the cylindrical samples for both tissue and printed inks were tested and compared for tissue 2 and ink 2, showing that the load–depth curves for tissue 2 and ink 2 overlap (Figure 2h). The difference is $\approx 0.1\%$ of the tissue hardness at the maximum nanoindenter load for these two specific test results (the difference is 7.8% of the tissue hardness for the average hardness values), indicating high fidelity. For quantitative analysis of the optical fidelity, optical reflections at the outer surface of the gross prostate tissue and ink 2 were compared (Figure 2i).^[25] Both the tissue and the ink possess the strongest reflection at wavelengths of 590–700 nm (orange and red), indicating good optical fidelity. Finally, the average density of the 3D printed model and inks was calculated to be 1.05 ± 0.07 g cm $^{-3}$, which is identical with human prostate tissue (1.05 g cm $^{-3}$).^[26]

Next, information about the prostate anatomy extracted from MRI scans (Movie S1, Supporting Information) was utilized to create a stereolithographic (STL) model and sliced into horizontal layers to generate G-code for the 3D printing process (Figure 3a) using our custom-built 3D printing system. Unlike conventional commercial 3D printers that use heating for extrusion of thermoplastic filaments, this setup uses adjustable pressure settings, which is better suited to handle the shear thinning properties of silicone-based polymeric inks at room temperature.^[27] The 3D printing process (Figure 3b and Movie S2, Supporting Information) follows the pathways dictated by the corresponding sliced STL model (Figure S3, Supporting Information) in order to generate the final 3D printed prostate model (Figure 3c). The printed models were typically left untouched for at least 1–3 days prior to performing the remaining experiments. A quantitative analysis of the organ model allowed us to quantify the fidelity of the anatomy between the 3D printed prostate model and its corresponding patient prostate. First, a 3D registration technique was used for surface comparison^[28] in order to analyze anatomical fidelity. The 3D printed prostate model was scanned by MRI, and then the MRI image stack (Figure 3d and Movie S3, Supporting Information) was utilized to generate an STL model. A calibrated distance map (Figure 3e) and a histogram of the calibrated distances (Figure 3f) of the corresponding points on the surface of the patient prostate model and 3D printed prostate model were generated via 3D registration. The results indicated that the anatomical difference for the outer surface (Figure 3e (left)) and inner urethra surface (Figure 3e (right)) is trivial, and most of the calibrated distance points scatter from -0.8 to 0.3 mm, with peaks close to 0 mm (Figure 3f). The overall anatomical fidelity was found to be 98% (Supporting Information).

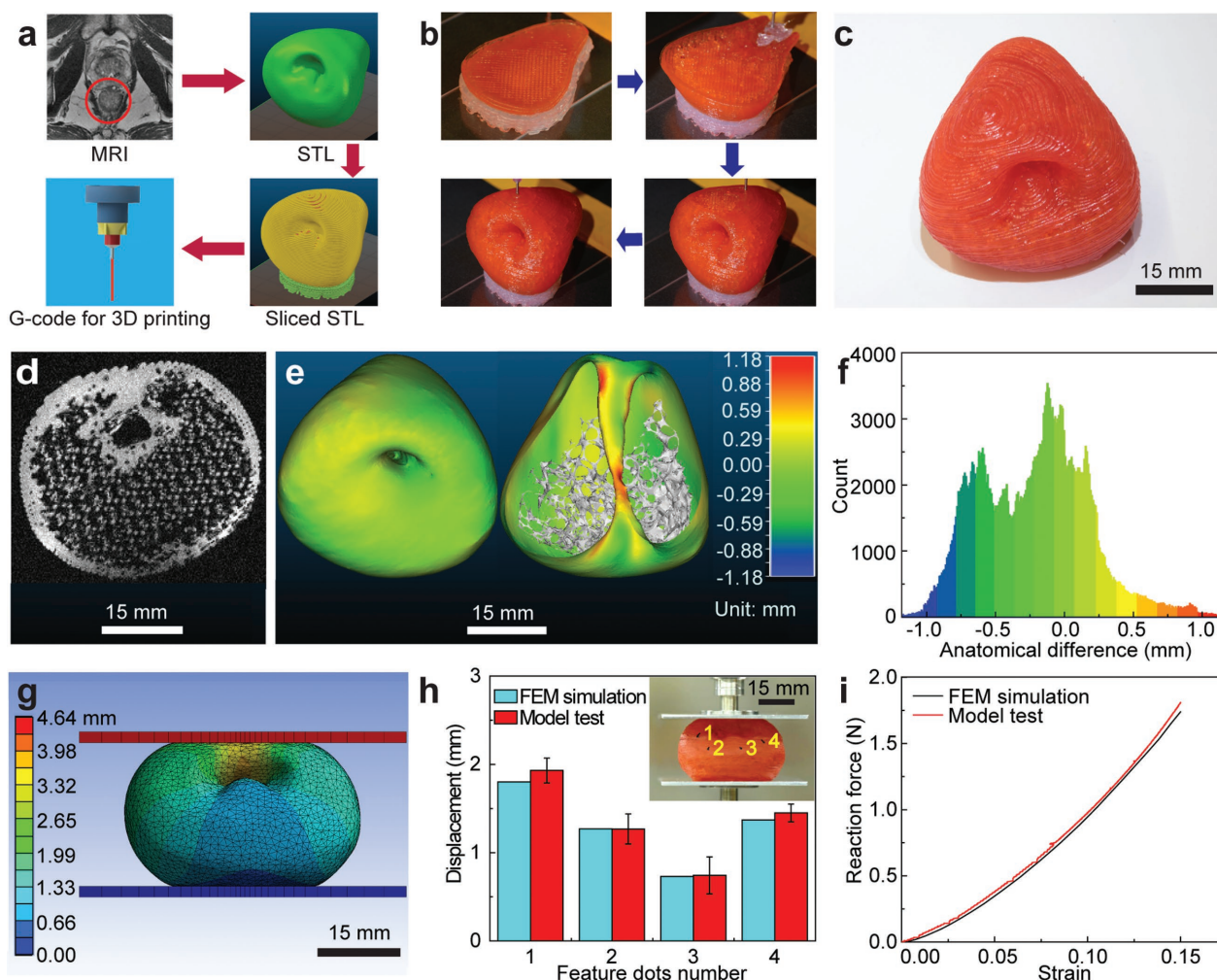


Figure 3. 3D printing of prostate model, anatomical fidelity analysis, and organ physical behavior prediction using the 3D printed prostate model. a) Procedure for converting patient-specific MRI to G-code for the 3D printing process. b) 3D printing process of the prostate model using the customized polymeric ink. c) Photograph of the 3D printed prostate model. d) An MRI image obtained via scanning a 3D printed prostate model. e) Calibrated distance map via 3D registration for comparison of anatomical fidelity between patient prostate and 3D printed prostate model at the outer surface (left) and urethra surface (right). f) Histogram of the calibrated distances of the surface points for comparison of anatomical fidelity between the patient prostate model and 3D printed prostate model. g) Total deformation results after compression of the FEM model (15% of model height). h) Displacement comparison for feature dots between results from compression of the 3D printed prostate model (with standard deviation error bars) and the FEM simulated model. Inset: Displacement of the feature dots on the 3D printed prostate model after compression with the displacement trajectories. i) Reaction force comparison between results from compression of the 3D printed prostate model and the FEM simulated model.

Next, considering the high fidelity of the ink properties and anatomical structure, the 3D printed prostate model can be used to predict the physical behavior of patient organs during surgical handling, which can help avoid the application of excessive deformation and force, and thus tissue damage during operation procedures. Our evaluation of organ physical behavior includes both FEM simulations of the patient organ and compression tests on the 3D printed prostate model (Figure S4a, Supporting Information). This procedure evaluates the predicted deformation of the 3D printed model both geometrically and mechanically.^[29–31] We selected an Ogden 3rd order model^[32,33] that fits the stress-strain curves of both the prostate tissue 2 and customized ink 2 for FEM simulation (Supporting Information) within the strain range of 0–0.15 (Figure S4b and Table S2, Supporting Information). We then simulated a compression process (15% of

entire model height, about 4.64 mm) via lowering the plate on top of the patient prostate model from its original state (Figure S4c, Supporting Information) and fixing the bottom plate. The different parts of the model showed varying deformation under the same applied compression (Figure 3g and Movie S4, Supporting Information). The reaction force of the model during compression was also predicted. The results from the FEM simulation provide a reference for organ physical behavior.

To demonstrate that the 3D printed prostate model can accurately and directly predict the organ physical behavior under compression, we designed a compression test by employing the 3D printed prostate model (Figure S4d, Supporting Information) under the same conditions as the simulation. A customized stereo system was designed to track the deformation of the prostate model (Figure S5, Supporting Information).^[34–39] The

displacement trajectories of four randomly selected feature dots were tracked on the model before (Figure S4d, Supporting Information) and after (Figure 3h Inset) the compression test process (Movie S5, Supporting Information). We then accurately located the feature dots on the FEM simulated model. A 3D scanned model (with surface texture) of the 3D printed prostate was matched to the original computer-aided design (CAD) model in order to register the feature dots in the FEM simulation (Figure S6, Supporting Information). Then, we read the displacement values for the dots from the simulated model. Finally, we compared the displacements of the dots in the compression test with the ones in the FEM simulation and found that the differences in average displacement for each dot were within 10% of simulation results (Figure 3h). In addition, the reaction force versus strain in the compression test was similar to the FEM simulation results (1.82 ± 0.11 N for the compression test and 1.74 N for the simulation at a strain of 0.15 , and 1.04 ± 0.06 N for the compression test and 1.02 N for the simulation at a strain of 0.10) (Figure 3i). These results demonstrate the feasibility of utilizing the 3D printed prostate model for organ physical behavior prediction.

We next sought to investigate the use of the 3D printed prostate models in surgical rehearsal simulations. We first applied an endoscope to enter the urethra of the 3D printed prostate model (Figure 4a and Figure S7, Supporting Information). To further enhance the effectiveness of the model as a surgical aid, we repeated this application with the prostate model embedded in a kidney–urethra–bladder model from the Center for Research in Education and Simulation Technologies (CREST)^[40] (Figure S8, Supporting Information). Due to the matching physical properties of the model with tissue, the endoscope can be easily inserted into the urethra to obtain an endoscopic view for any region of the surface, even under conditions of pressing or squeezing (Figure 4b and Movie S6, Supporting Information). The endoscopic view from the 3D printed prostate model showed the unfilled prostatic urethra in the patient's MRI which was neither dilated by the endoscope nor filled by irrigating fluid and urine. Thus, this application suggests the effectiveness of these organ models in assisting medical professionals for more efficient planning and rehearsal from organ inner channels via the use of an endoscope. In addition, we conducted a suturing experiment on the 3D printed prostate model with the aid of a surgeon (Figure 4c and Movie S7, Supporting Information). Although this is not a common practice for the prostate organ, it indicated that the 3D printed models exhibited sufficiently good strength to avoid excessive damage during invasive surgical procedures, such as needle penetration. Furthermore, feedback from the surgeon indicated that 3D printed prostate model remained robust during suturing, it did not exhibit any tearing, and the surgical knot did not pull through.

Next, we 3D printed soft capacitive tactile sensors^[41] for incorporation onto the 3D printed prostate model with the purpose of offering quantitative sensing capabilities via conformal integration. The sensor consists of a polyacrylamide-based ionic hydrogel and a silicone-based dielectric elastomer (Figure 4d), which were used as the electrodes and electroactive component of the sensor, respectively.^[41,42] The hydrogel electrodes and the dielectric elastomer layer have elastic moduli of 11.05 ± 2.97 and 75.47 ± 12.65 kPa at 100% strain rate,

respectively. In addition, they possess shear thinning properties, which facilitates the 3D printing process. We also added silicone layers on the top and bottom of the device to facilitate its handling and longevity. The final 3D printed device has dimensions of $10 \times 10 \times 1.2$ mm³ ($L \times W \times H$). Upon the application of external pressure to the sensor, the dielectric elastomer experiences a deformation (compression of thickness and expansion in area), which results in a change in device capacitance.^[41,42] After printing, the sensor was calibrated using pin compression under various applied pressures (Figure S9, Supporting Information). The response of the tactile sensor exhibited excellent repeatability in terms of capacitance change under applied pressure (Figure 4e, under 50 kPa of applied pressure as a demonstration example). The capacitance change and the applied pressure showed a linear correlation at a pressure range of 20–120 kPa (Figure 4f). This calibration data can be used to calculate the pressure applied to the tactile sensor via corresponding changes in capacitance.

We designed and conducted quantitative surgical rehearsal applications using the 3D printed prostate model with the integrated 3D printed sensors. These applications aim to train medical professionals to quantitatively realize and control the amount of applied pressure and its duration within reasonable ranges before operating on patient organs. For each application, we applied three quick press–release and three press–hold–release cycles using either a finger or surgical and diagnostic tools on the sensor. For the first application example, we integrated the sensor on the outer surface of the model. Then we applied finger pressing, a surgical grasper, and surgical scissors to the sensor and deduced their corresponding pressure responses from the capacitance changes (Figure 4g,h and Figure S10a, Supporting Information). For the second application example, we integrated the sensor on the urethra surface of the model. Then, we used an endoscope, surgical grasper, and surgical scissors on the sensor and deduced their corresponding pressure responses from the capacitance changes (Figure 4i,j and Figure S10b, Supporting Information). The real-time applications and corresponding capacitance changes of the sensor in the first and second application examples are shown in Figure S11 and Movies S8–S13 in the Supporting Information.

In summary, we have designed and developed a series of novel methodologies and customized inks for fabricating a 3D printed prostate model with physical properties of tissue and integrated sensing capabilities that can be used for quantitative, advanced surgical rehearsal. The 3D printed prostate model demonstrated high fidelity with patient organ and tissue in anatomical, static and dynamic mechanical, hardness, and optical properties. Therefore, the prostate model can aid medical professionals to perform more effective preoperative planning and rehearsal and predict organ physical behavior more accurately. The tissue-like tactile sensation can help to hone surgical skills for training purposes. In addition, the flexible urethra provides the possibility of practicing with tools within organ channels. Finally, conformal integration of 3D printed soft tactile sensors on the surface of the 3D printed prostate model allows the model to exhibit quantitative feedback. Future studies will focus on several different directions, including: (1) fabrication of organ models with heterogeneous properties, durometers,

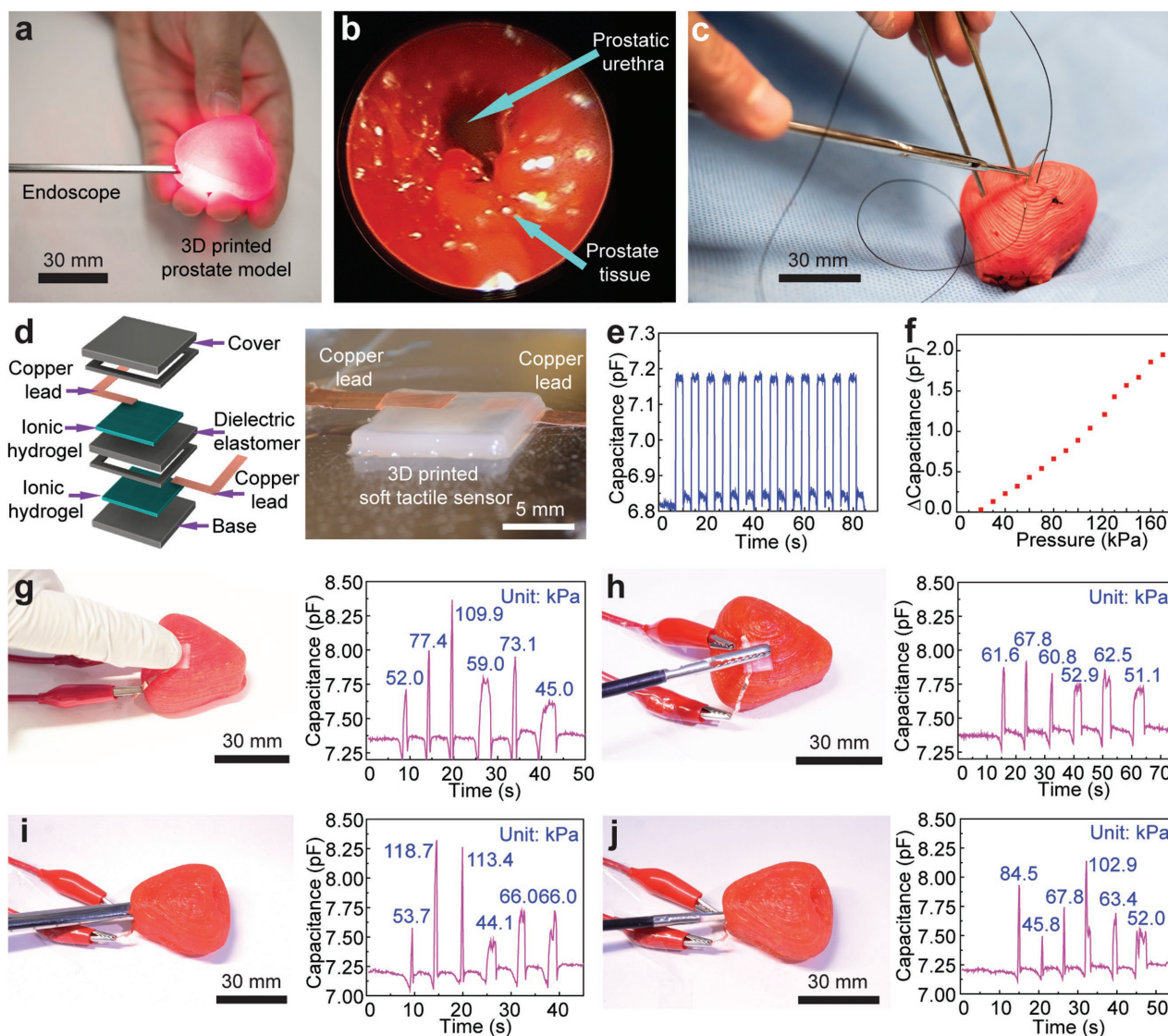


Figure 4. Quantitative surgical rehearsal using the 3D printed prostate model. a) Surgical rehearsal involving applying an endoscope in the urethra of the 3D printed prostate model. b) Endoscopic view of the urethra inside of the 3D printed prostate model. c) Surgical suturing on the 3D printed prostate model. d) Schematic of the structure of the 3D printed soft tactile sensor (left) and photograph of the corresponding 3D printed sensor (right). e) Characterization of the response repeatability for the soft tactile sensor via capacitance changes with an applied cyclic pressure of 50 kPa. f) Calibration of the 3D printed sensor based on the correlation between capacitance change and the applied pressure. Quantitative surgical rehearsal involving the 3D printed prostate model upon applying a finger g) and a surgical grasper h), respectively, on the sensor integrated on the outer surface of the model and their corresponding pressure responses (indicated at each of the peaks) from the capacitance changes of the sensor. Quantitative surgical rehearsal involving the 3D printed prostate model when applying an endoscope i) and surgical scissors j) on the sensor integrated on the urethra surface inside of the model, and their corresponding pressure responses (indicated at each of the peaks) from the capacitance changes of the sensor.

and dynamic functionalities; (2) direct integration of 3D printed electronics for multidimensional feedback; (3) incorporation of virtual and assisted reality tools; (4) evaluation of this work in real use cases for patient safety and surgical outcomes; and (5) manipulation of anisotropic properties of the different organ models, since previous work has shown that by controlling the orientation of printing pathways^[43,44] and imbedding fillers,^[45,46] anisotropic properties can be introduced into 3D printed materials and models. Overall, we believe that the concept of creating 3D printed patient-specific organ models with anatomical accuracy, physical properties of tissue, and

integrated 3D printed soft electronics suggests a new paradigm in preoperative practice.

Experimental Section

Fabrication of Customized Polymeric Inks with Physical Properties of Tissue for 3D Printing: Silicone sealant (acetoxo-based RTV sealant Loctite SI 595 CL), silicone grease (#LP20, Trident), Procylinyl Red GS (ICI America Inc.), and fumed silica (7 nm, Aldrich) were combined in the formulation as an active agent for vulcanization, a bulking agent (softness after vulcanization), a coloring agent, and a thickening agent,

respectively. The active agent and the bulking agent were mixed at proper weight ratios (Figure 2c and Table S1, Supporting Information) to achieve different values of Young's modulus via a mixer (ARE-310, Thinky) to form the primary component of the customized polymeric inks.

3D Printing of Organ Models: The MRI image pack (1 mm resolution) of the patient prostate organ was processed to generate G-code for printing using a custom-built 3D printing system (AGS 100, Aerotech). The customized polymeric ink and supporting ink (Loctite SI 595 CL) were deposited from two dispensing apparatuses. The supporting ink was removed mechanically after the inks in the model were fully cured. For more complex organ models, the supporting ink can be replaced with 33 wt% Pluronic F-127 (Sigma-Aldrich) in water. The supporting ink can then be easily removed via flushing with water at 4°C.

Characterization of Prostate Tissue and Customized Polymeric Inks: The human prostate was collected using radical prostatectomy. The tissue was cut into cylindrical samples for testing. The customized polymeric inks were 3D printed into cylindrical samples for direct comparison of results. Static and dynamic compression tests were carried out using a mechanical analyzer (RSA-G2, TA Instruments). The hardness tests were conducted on a nanoindentation system (Nanoindenter XP, MTS). For optical reflection tests, the gross tissue and colored 3D printed samples were evaluated using fiber optic equipment (Ocean Optics).

Rheological Characterization: The rheology of the customized polymeric ink and its corresponding active and bulking agents was characterized on a magnetic bearing rheometer (AR-G2, TA Instruments).

MRI of 3D Printed Prostate Model: Imaging of the 3D printed prostate model was carried out using an MRI system (9.4 Tesla) while the 3D printed prostate model was placed in a 31 cm bore (Magnex Scientific).

3D Registration for Anatomical Fidelity: 3D registration of the STL files between the 3D printed prostate model and the patient prostate model was achieved using CloudCompare software.

FEM Simulation: The FEM software employed for simulation was ANSYS Workbench 17.1 and the component was Static Structural. An Ogden third model was used to fit the measured strain–stress data. The simulation setup was configured to be identical to the compression test. The contacts between the FEM model and plates were defined as frictional with a friction coefficient of 10, and 137 905 nodes were generated for the model with a size of 45.14 mm × 41.70 mm × 30.95 mm (L × W × H). In the mesh section, the element size of the prostate model was set to be 3 mm, and the surface size of the contacting areas with the top and bottom plates was set to be 1 mm. The top and bottom plates were meshed by sweeping in the Z-axis with one division separately, and the edges were divided into 20 segments each with a bias factor of 5. The element types were determined via ANSYS Workbench.

3D Displacement Measurement Using Stereo System with Feature Dots During Model Compression: A 3D displacement measurement procedure based on a stereo system was designed and applied to track the 3D trajectories of the feature dots on the 3D printed prostate model (ink 2, 100% fill density) during model compression by a mechanical analyzer (RSA-G2, TA Instruments). The reaction force was also read from the mechanical analyzer.

Mapping of the Feature Dots to the Corresponding Locations on the FEM Simulation Model: A 3D printed prostate model with feature dots was coated with a thin layer of baby powder for 3D scanning (HDI 109, GoMeasure3D). The scanned model and the FEM simulation model were then imported into the CloudCompare software for 3D registration with a uniform coordinate system. The location coordinates (x, y, z) of the feature dots on the scanned model were used to map the corresponding locations with the same coordinates on the FEM simulation model.

3D Printing and Calibration of Soft Tactile Sensor: A soft capacitive sensor device was 3D printed by alternately depositing layers of two different materials (polyacrylamide-based ionic hydrogel and silicone-based dielectric elastomer), followed by their photopolymerization via exposure to a UV system (Omnicure S1500, Excelitas Technologies). The soft sensor was then calibrated by applying varying pressures to the device and measuring the changes in capacitance.

Advanced Surgical Rehearsal Using the 3D Printed Prostate Model: (1) An endoscope was inserted into the urethra of the model and the endoscopic view was observed from the surgical display in the endoscopic tower station (Stryker). (2) Surgical suturing was conducted on the surface of the 3D printed prostate model with the assistance of a surgeon and by utilizing a surgical needle for penetration and surgical thread (ETHICON) for suturing. (3) Finger, surgical, and diagnostic tools were applied on the sensors integrated on the surface and interior of the 3D printed prostate model. For each application, three quick press–release and three press–hold–release cycles were applied. The signal responses of capacitance changes of the sensor were then converted into values of applied pressures via sensor calibration data.

Experimental details for procedures and parameter settings as well as theoretical models can be found in the Supporting Information.

Supporting Information

Supporting Information is available from the Wiley Online Library or from the author.

Acknowledgements

M.C.M. acknowledges the National Institute of Biomedical Imaging and Bioengineering of the National Institutes of Health (Award No. 1DP2EB020537), and the Army Research Office for the development of the 3D printed soft sensor (Award No. W911NF-15-1-0469). B.M.O. acknowledges support by the National Heart, Lung, and Blood Institute of the National Institutes of Health (Award No. R01HL137204). The content is solely the responsibility of the authors and does not necessarily represent the official views of the National Institutes of Health. R.M.S. and B.R.K. acknowledge support from the Department of Urology at the University of Minnesota (UMN). C.-C.C. acknowledges support from the Rebecca Q. Morgan Foundation. The authors thank D. Sciacca and S. Krishna from the UMN Medical School for their assistance in acquiring prostate tissue. The authors thank Dr. D. Giles from the UMN Polymer Characterization Facility and L. M. Tenorio from UMN Biomedical Engineering for mechanical test support. The authors also thank Dr. J. Nelson from the UMN Characterization Facility and Dr. D. Nedrelov from the UMN Tissue Mechanics Lab for assistance with hardness tests. The authors thank J. Lee from UMN Biomedical Engineering for optical test support. The authors thank T. Reihisen, L. H. Poniatowski, and D. Burke from the University of Washington (UW) Department of Urology for tissue testing, organ MRI processing, and medical application and material suggestions. The authors thank Dr. D. Idiyatullin from UMN Center for Magnetic Resonance Research (CMMR), Department of Radiology for assistance with acquiring the MRI for the 3D printed prostate model. The authors thank J. Graff from UMN SimPORTAL for assistance with using the endoscope tower station. The authors thank N. J. Bibus from the UMN Medical Center for assistance with acquiring surgical and diagnostic tools. The authors thank Dr. J. Gorman from UMN Mechanical Engineering and J. Malluege from ANSYS, Inc. for FEM simulation assistance. The authors thank S. Thomalla from the Medical Device Center for help with commercial material printing for comparison purposes. The authors also thank Dr. D. Joung, D. Yang, and B. Bogdalek from UMN Mechanical Engineering, for their valuable comments and suggestions during paper preparation. An Institutional Review Board (IRB) review at the University of Minnesota determined that this experiment does not meet the federal definition of human subjects research and, therefore, an IRB review was not required.

Conflict of Interest

The authors declare no conflict of interest.

Keywords

3D printed sensors, 3D printing, organ models, soft materials, surgical aids

Received: August 31, 2017

Revised: October 4, 2017

Published online: December 6, 2017

- [1] M. A. Makary, M. Daniel, *BMJ* **2016**, 353, i2139.
- [2] C. A. Thiels, T. M. Lal, J. M. Nienow, K. S. Pasupathy, R. C. Blocker, J. M. Aho, T. I. Morgenthaler, R. R. Cima, S. Hallbeck, J. Bingener, *Surgery* **2015**, 158, 515.
- [3] J. McGhee, *J. Anat.* **2010**, 216, 264.
- [4] G. An, L. Hong, X.-B. Zhou, Q. Yang, M.-Q. Li, X.-Y. Tang, *Ann. Anat.* **2017**, 210, 76.
- [5] F. Adams, T. Qiu, A. Mark, B. Fritz, L. Kramer, D. Schlager, U. Wetterauer, A. Miernik, P. Fischer, *Annu. Biomed. Eng.* **2017**, 45, 963.
- [6] N. Kadoya, Y. Miyasaka, Y. Nakajima, Y. Kuroda, K. Ito, M. Chiba, K. Sato, S. Dobashi, T. Yamamoto, N. Takahashi, M. Kubozono, K. Takeda, K. Jingu, *Med. Phys.* **2017**, 44, 1445.
- [7] F. Rengier, A. Mehndiratta, H. von Tengg-Kobligk, C. M. Zechmann, R. Unterhinninghofen, H.-U. Kauczor, F. L. Giesel, *Int. J. Comput. Assist. Radiol. Surg.* **2010**, 5, 335.
- [8] K. M. Farooqi, C. G. Lengua, A. D. Weinberg, J. C. Nielsen, J. Sanz, *Pediatr. Cardiol.* **2016**, 37, 1028.
- [9] N. Wake, H. Chandarana, W. C. Huang, S. S. Taneja, A. B. Rosenkrantz, *Clin. Radiol.* **2016**, 71, 610.
- [10] N. N. Zein, I. A. Hanouneh, P. D. Bishop, M. Samaan, B. Egtesad, C. Quintini, C. Miller, L. Yerian, R. Klatte, *Liver Transplant.* **2013**, 19, 1304.
- [11] Y. Komai, M. Sugimoto, N. Gotohda, N. Matsubara, T. Kobayashi, Y. Sakai, Y. Shiga, N. Saito, *Urology* **2016**, 91, 226.
- [12] M. Kusaka, M. Sugimoto, N. Fukami, H. Sasaki, M. Takenaka, T. Anraku, T. Ito, T. Kenmochi, R. Shiroki, K. Hoshinaga, *Transplant. Proc.* **2015**, 47, 596.
- [13] S. Mottl-Link, M. Hübler, T. Kühne, U. Rietdorf, J. J. Krueger, B. Schnackenburg, R. De Simone, F. Berger, A. Juraszek, H.-P. Meinzer, M. Karck, R. Hetzer, I. Wolf, *Ann. Thorac. Surg.* **2008**, 86, 273.
- [14] G. Gómez-Ciriza, T. Hussain, T. Gómez-Cía, I. Valverde, *Interv. Cardiol.* **2015**, 7, 343.
- [15] S. Hassanipour-Azgom, A. Mohammadian-Hafshejani, M. Ghoncheh, F. Towhidi, S. Jamehshorani, H. Salehiniya, *Prostate Int.* **2016**, 4, 118.
- [16] G. A. Schuster, T. G. Schuster, *J. Urol.* **1999**, 161, 1168.
- [17] P. A. Huijing, *J. Biomech.* **1999**, 32, 329.
- [18] J. T. Muth, D. M. Vogt, R. L. Truby, Y. Mengüç, D. B. Kolesky, R. J. Wood, J. A. Lewis, *Adv. Mater.* **2014**, 26, 6307.
- [19] P. N. T. Wells, H.-D. Liang, *J. R. Soc. Interface* **2011**, 8, 1521.
- [20] T. A. Krouskop, T. M. Wheeler, F. Kallel, B. S. Garra, T. Hall, *Ultrason. Imaging* **1998**, 20, 260.
- [21] R. J. DeWall, T. Varghese, M. A. Kliewer, J. M. Harter, E. M. Hartenbach, *Ultrason. Imaging* **2010**, 32, 214.
- [22] M. Zhang, P. Nigwekar, B. Castaneda, K. Hoyt, J. V. Joseph, A. di Sant'Agnese, E. M. Messing, J. G. Strang, D. J. Rubens, K. J. Parker, *Ultrasound Med. Biol.* **2008**, 34, 1033.
- [23] D. M. Ebenstein, L. A. Pruitt, *J. Biomed. Mater. Res., Part A* **2004**, 69A, 222.
- [24] P. K. Zysset, X. Edward Guo, C. Edward Hoffer, K. E. Moore, S. A. Goldstein, *J. Biomech.* **1999**, 32, 1005.
- [25] T. J. Bruno, P. D. N. Svoronos, *CRC Handbook of Fundamental Spectroscopic Correlation Charts*, CRC Press, Boca Raton, FL **2005**.
- [26] I. Karademir, D. Shen, Y. Peng, S. Liao, Y. Jiang, A. Yousuf, G. Karczmar, S. Sammet, S. Wang, M. Medved, T. Antic, S. Eggener, A. Oto, *AJR Am. J. Roentgenol.* **2013**, 201, 1041.
- [27] S.-Z. Guo, K. Qiu, F. Meng, S. H. Park, M. C. McAlpine, *Adv. Mater.* **2017**, 29, 1701218.
- [28] W. Shui, M. Zhou, S. Chen, Z. Pan, Q. Deng, Y. Yao, H. Pan, T. He, X. Wang, *Int. J. Comput. Assist. Radiol. Surg.* **2017**, 12, 13.
- [29] M. R. McCurry, A. R. Evans, C. R. McHenry, *PeerJ* **2015**, 3, e988.
- [30] G. A. Holzapfel, T. C. Gasser, M. Stadler, *Eur. J. Mech. A/Solids* **2002**, 21, 441.
- [31] K. K. Brock, M. B. Sharpe, L. A. Dawson, S. M. Kim, D. A. Jaffray, *Med. Phys.* **2005**, 32, 1647.
- [32] R. W. Ogden, *Proc. R. Soc. A* **1972**, 326, 565.
- [33] B. Kim, S. B. Lee, J. Lee, S. Cho, H. Park, S. Yeom, S. H. Park, *Int. J. Precis. Eng. Manuf.* **2012**, 13, 759.
- [34] J.-Y. Bouguet, *Camera Calibration Toolbox for Matlab* (California Institute of Technology, http://www.vision.caltech.edu/bouguetj/calib_doc/) **2004**.
- [35] J. Heikkilä, O. Silven, presented at *Proc. 13th Int. Conf. Pattern Recognit.*, Vienna, Austria, August **1996**.
- [36] J. Heikkilä, O. Silvén, presented at *IEEE Comput. Soc. Conf. Comput. Vision Pattern Recognit.*, San Juan, Puerto Rico, USA, June **1997**.
- [37] Z. Zhang, presented at *Proc. 7th IEEE Int. Conf. Comput. Vision, Kerkyra*, Greece, September **1999**.
- [38] C. B. Duane, *Photogramm. Eng.* **1971**, 37, 855.
- [39] J. G. Fryer, D. C. Brown, *Photogramm. Eng. Remote Sens.* **1986**, 52, 51.
- [40] R. M. Sweet, *J. Endourol.* **2016**, 31, S69.
- [41] S. S. Robinson, K. W. O'Brien, H. Zhao, B. N. Peele, C. M. Larson, B. C. Mac Murray, I. M. Van Meerbeek, S. N. Dunham, R. F. Shepherd, *Extreme Mech. Lett.* **2015**, 5, 47.
- [42] J.-Y. Sun, C. Keplinger, G. M. Whitesides, Z. Suo, *Adv. Mater.* **2014**, 26, 7608.
- [43] B. N. Johnson, K. Z. Lancaster, G. Zhen, J. He, M. K. Gupta, Y. L. Kong, E. A. Engel, K. D. Krick, A. Ju, F. Meng, L. W. Enquist, X. Jia, M. C. McAlpine, *Adv. Funct. Mater.* **2015**, 25, 6205.
- [44] R. Zou, Y. Xia, S. Liu, P. Hu, W. Hou, Q. Hu, C. Shan, *Composites, Part B* **2016**, 99, 506.
- [45] K. Gnanasekaran, T. Heijmans, S. van Bennekom, H. Woldhuis, S. Wijnia, G. de With, H. Friedrich, *Appl. Mater. Today* **2017**, 9, 21.
- [46] A. D. Valentine, T. A. Busbee, J. W. Boley, J. R. Raney, A. Chortos, A. Kotikian, J. D. Berrigan, M. F. Durstock, J. A. Lewis, *Adv. Mater.* **2017**, 29, 1703817.

**ADVANCED
MATERIALS
TECHNOLOGIES**

Supporting Information

for *Adv. Mater. Technol.*, DOI: 10.1002/admt.201700235

3D Printed Organ Models with Physical Properties of Tissue
and Integrated Sensors

Kaiyan Qiu, Zichen Zhao, Ghazaleh Haghtashtiani, Shuang-Zhuang Guo, Mingyu He, Ruitao Su, Zhijie Zhu, Didarul B. Bhuiyan, Paari Murugan, Fanben Meng, Sung Hyun Park, Chih-Chang Chu, Brenda M. Ogle, Daniel A. Saltzman, Badrinath R. Konety, Robert M. Sweet, and Michael C. McAlpine**

Supporting Information

3D Printed Organ Models with Physical Properties of Tissue and Integrated Sensors

Kaiyan Qiu, Zichen Zhao, Ghazaleh Haghighashtiani, Shuang-Zhuang Guo, Mingyu He, Ruitao Su, Zhijie Zhu, Didarul B. Bhuiyan, Paari Murugan, Fanben Meng, Sung Hyun Park, Chih-Chang Chu, Brenda M. Ogle, Daniel A. Saltzman, Badrinath R. Konety, Robert M. Sweet, and Michael C. McAlpine**

Dr. K. Qiu, G. Haghighashtiani, Dr. S.-Z. Guo, R. Su, Z. Zhu, Dr. F. Meng, Dr. S. H. Park, and Prof. M. C. McAlpine

Department of Mechanical Engineering, University of Minnesota, Minneapolis, Minnesota 55455, United States

E-mail: mcalpine@umn.edu

Dr. Z. Zhao and Prof. R. M. Sweet

WWAMI Institute for Simulation in Healthcare, University of Washington, Seattle, Washington 98195, United States

E-mail: rsweet@uw.edu

Dr. Z. Zhao, Prof. B. R. Konety, and Prof. R. M. Sweet

Department of Urology, University of Minnesota, Minneapolis, Minnesota 55455, United States

Dr. M. He, and Prof. C. C. Chu

Fiber Science & Biomedical Engineering Programs, Cornell University, Ithaca, New York 14853, United States

Dr. D. B. Bhuiyan, and Prof. B. M. Ogle

Department of Biomedical Engineering, University of Minnesota, Minneapolis, Minnesota 55455, United States

Prof. P. Murugan

Department of Laboratory Medicine and Pathology, University of Minnesota, Minneapolis, Minnesota 55455, United States

Prof. D. A. Saltzman

Department of Surgery, University of Minnesota, Minneapolis, Minnesota 55455, United States

Experimental Details

1. Fabrication of customized polymeric inks with physical properties of tissue for 3D printing

The ink formulation consists of active agent: silicone sealant (Loctite SI 595TM CL with acetoxy-based room temperature vulcanization formulation), bulking agent: silicone grease (#LP20, Trident[®]), coloring agent: Procyinyl Red GS (ICI America Inc.) and thickening agent: fumed silica (powder 7 nm, Aldrich). The active agent and bulking agent were mixed at proper weight ratios via a mixer (ARE-310, Thinky) at 2,000 rpm for 10 mins to form the customized polymeric inks with different mechanical properties. The weight ratio of active agent to bulking agent for inks 1, 2, 3 are ca. 0.95:3.05, 0.90:3.10, and 0.82:3.18, respectively, to achieve different values of Young's modulus, and the ratio values can be slightly varied for fine-tuning mechanical properties in different batches. The customized polymeric inks (10 g) were then mixed with 1% (w/v) coloring agent DCM solution (0.5 mL) at 20:1 (w/v) ratio via the mixer at 2,000 rpm for 10 mins. DCM solvent was removed from the customized polymeric inks via vacuum before use. Trivial amount of the thickening agent was added in a few of the formulations, if the viscosity of the precursor needed to be elevated to achieve proper printability.

2. 3D printing of organ models

The MRI image pack (1 mm resolution) of a patient organ (prostate) was edited via Vitrea[®] software to form a patient organ (prostate) STL model. The STL model was then sliced via Slic3r open source software to generate G-code for printing using a custom-built 3D printing system (AGS 100, Aerotech) with two independent *z-axis* heads. The customized polymeric ink and supporting ink (Loctite SI 595TM CL) were deposited from two dispensing apparatuses controlled by two high precision dispensers (Ultimus V, EFD) through nozzles with 610 μm inner diameters (20 GA GP.023X.25, EFD) and 500 μm layer heights. The supporting ink was removed after the model was fully cured at ambient temperature in air. For more complex organ models, the supporting ink can be replaced with 33 wt% Pluronic[®] F-

127 (Sigma-Aldrich) in water. The supporting ink can then be easily removed via flushing with water at 4 °C. The resolution of the model can be adjusted by changing the nozzle sizes.

3. Characterization tests for prostate tissue and customized polymeric inks

The human prostate was collected immediately following radical prostatectomy. The tissue was cut into approximately 8 mm × 5 mm (D × H) cylindrical samples with flat surfaces via a surgical punch biopsy instrument with a circular hollow blade (8 mm diameter) for static/dynamic compression and hardness tests. The customized polymeric inks were 3D printed into cylindrical samples with similar dimensions as the tissue samples for comparison. Both static and dynamic compression tests were carried out using a mechanical analyzer (RSA-G2, TA) while the tissue samples were placed on the paten. The static compression tests were conducted for up to 0.20 strain at a rate of 0.1 s⁻¹ (0.5 mm/s). The dynamic compression tests were conducted at frequencies of 0.1-20 Hz and at strains of 0.05, 0.10, and 0.20. The hardness tests were conducted on a nanoindentation system (Nanoindenter XP, MTS) at a strain rate of 0.5 s⁻¹ for both loading and unloading with a depth limit of 20 μm. For optical reflection tests, the outer gross tissue of prostate and colored 3D printed samples were directly evaluated using fiber optic equipment (Ocean Optics) within a visible light wavelength range of 390-700 nm.

4. Rheological characterization

The rheology characterization of the customized polymeric ink and its corresponding active agent and bulking agent components were performed on a magnetic bearing rheometer (AR-G2, TA Instruments) with a steel plate (25 mm diameter) in Smart Swap geometry at 25 °C. Flow experiments were conducted via a logarithmic sweep of shear rate at 0.1-1000 s⁻¹ with a 500 μm gap between the Smart Swap geometry and the lower geometry.

5. MRI of 3D printed prostate model

Imaging was carried out using an MRI system (9.4 Tesla), while the 3D printed prostate model was placed in a 31 cm bore (Magnex Scientific). The field of view (FOV) was set to 5 mm × 5 mm × 5 mm. The number of scans and views were set to 200 and 128,000, respectively.

6. 3D registration for anatomical fidelity

A 3D model of the printed prostate was obtained from the MRI image stack using the Mimics software package. 3D registration of the STL files between the 3D printed prostate model and the patient prostate model was achieved using CloudCompare open source software.

CloudCompare was also used to obtain a distance map and a histogram of the distances of the corresponding points on the surface for the overlaid 3D models, using a comparison of 3×10^5 data points on the surface in 40 iterations. The arbitrary distance scale generated by CloudCompare was calibrated to mm scale and the root-mean-square (RMS) value for the histogram was obtained (0.45 mm). By comparing the RMS value of the calibrated distances with the highest dimension of the patient prostate model (22.33 mm), the error in the printing process was obtained (0.02). The quantitative fidelity (98%) was obtained by deducting the error value in printing from 100%.

7. FEM simulation

The FEM software employed for this research was ANSYS Workbench 17.1 and the used component was “Static Structural.” The first step of the simulation was to create a material model that was assigned to the prostate geometry in the subsequent step. The density of the ink was set to be 1.05 mg/ml for human prostate tissue. The uniaxial compression strain-stress relationship of the prostate tissue was added to the engineering data in a table format. A third order Ogden hyperelastic model^[1] was employed to fit the data and generate the strain-stress curve (Figure S4b). The strain energy density function for the third order Ogden hyperelastic model is:

$$\begin{aligned} \psi = & \frac{\mu_1}{\alpha_1}(\lambda_1^{\alpha_1} + \lambda_2^{\alpha_2} + \lambda_3^{\alpha_3} - 3) + \frac{\mu_2}{\alpha_2}(\lambda_1^{\alpha_1} + \lambda_2^{\alpha_2} + \lambda_3^{\alpha_3} - 3) \\ & + \frac{\mu_3}{\alpha_3}(\lambda_1^{\alpha_1} + \lambda_2^{\alpha_2} + \lambda_3^{\alpha_3} - 3) + \frac{1}{d_1}(J - 1)^2 + \frac{1}{d_2}(J - 1)^4 + \frac{1}{d_3}(J - 1)^6 \end{aligned} \quad (S1)$$

where λ_p ($p = 1, 2, 3$) are the deviatoric principal stretches of the Left Cauchy-Green tensor (in the case of uniaxial test $\lambda_2 = \lambda_3 = 0$), J is the determinant of the elastic deformation gradient, and μ_p , α_p and d_p are material constants which can be retrieved from the input data.

The initial shear modulus is given as:

$$\mu = \frac{1}{2}(\alpha_1\mu_1 + \alpha_2\mu_2 + \alpha_3\mu_3) \quad (S2)$$

and the initial bulk modulus is:

$$K = \frac{2}{d_1} \quad (S3)$$

The strain-stress relation derived from this model is:

$$\sigma = \sum_{p=1}^3 \mu_p [(1 + \varepsilon)^{\alpha_p - 1} - (1 + \varepsilon)^{-\frac{1}{2}\alpha_p - 1}] \quad (S4)$$

where σ is stress and ε is strain; in the case of compressive deformation, $1 + \varepsilon = \lambda$.

The geometric model of the prostate was obtained from the MRI scan of a human prostate and was exported as an STL file which was then imported into MeshLab to reduce the number of surfaces to 5,000. In order to generate an identical initial orientation between the geometric model and the printed model in the following compression test, a 2 mm section was cut and removed from the bottom of the geometric model to form a flat plane and make it stably sit on the bottom plate. The geometry had a size of 45.14 mm \times 41.70 mm \times 30.95 mm (L \times W \times H). The simplified geometry was resaved as a SolidWorks part file, which can then be imported into ANSYS Workbench 17.1. After importing the SolidWorks part file into the ‘‘Geometry Modeler’’ section, two plates with the same size of 60 mm \times 60 mm \times 2 mm (L \times W \times H) were created contacting the top and bottom boundaries of the prostate model. In the ‘‘Model’’ section, structural steel was assigned to these two plates, and tested tissue data fitted

by the Ogden third order model was assigned to the prostate. The contacting interfaces between the prostate and the testing plates were defined as frictional, with a friction coefficient of 10 to avoid sliding of the model on the plates. 137,905 nodes were generated after meshing the three geometries with the interfacial surface meshing size being 0.7 mm. In the mesh section, the element size of the prostate model was set to be 3 mm, and the surface size of the contacting areas with the top and bottom plates was set to be 1 mm. The top and bottom plates were meshed by sweeping in the Z-axis with one division separately, and the edges were divided into 20 segments each with a bias factor of 5. The element types were determined via ANSYS Workbench. A displacement of about 4.64 mm from the original position in the $-Z$ direction was assigned to the top plate, and the bottom plate was set as fixed to compress the prostate model for about 15.0% of its height. A total compression time of 9.28 seconds was set to make the simulation speed the same as the actual testing speed. After the solution was complete, total deformation (3D displacement) of the feature dots was extracted. Reaction force (up to 1.74 N at 15%) for the entire compression in the $-Z$ direction from the top plate was also recorded.

8. 3D displacement measurement using stereo system during model compression test

In order to track 3D trajectories of the feature points on the 3D printed prostate model during the compressing process, a 3D displacement measurement procedure based on a dual camera stereo system was designed and applied. The advantages of using a computer stereo vision approach to capture the 3D spatial information include: tracking 2D patterns on a smooth surface without identifiable 3D features, monitoring 3D deformation with high-frequency data sampling, customizing the system with good flexibility and off-the-shelf equipment, and good portability.

8.1. Notations. The vectors are expressed with bold and skew letters in lower case, while the matrices are expressed with bold letters in upper case. The frames mentioned here are in 3D spaces by default, each with an origin and three orthogonal coordinates (x , y and z). As with

the subscript and superscript notations, given two frames $\{A\}, \{B\}$ in 3D space, ${}^A\mathbf{p}_B \in \mathbb{R}^{3 \times 1}$ and ${}^A\mathbf{C}_B \in SO(3)$ denote the translation and rotation from frame B to frame A, respectively.

For any point ${}^A\mathbf{q}$ expressed in frame A, its expression can be found in frame B by

$${}^B\mathbf{q} = {}^B\mathbf{p}_A + {}^B\mathbf{C}_A {}^A\mathbf{q} \quad (\text{S5})$$

8.2. Hardware setup. The surface of the 3D printed prostate model (printed based on the modified geometric model in FEM simulation for comparison) was marked with four black points as feature dots, whose trajectories during the compression test were monitored by the stereo vision system. Before setting up the hardware for 3D displacement measurement, the marked model (ink 2, 100% fill density) was set up on the mechanical analyzer (RSA-G2, TA), between two aluminum plates (60 mm \times 60 mm \times 2 mm [L \times W \times H]), according to the requirement of the compression test procedure. To prevent the sticking of the model to the plates during the test due to inherent tackiness of the material, baby powder (Johnson & Johnson) was applied to the contact surface of the marked model. Two Nikon cameras (D750) with lenses (Nikon AF Micro NIKKOR 200mm f/4D) were mounted on a single tripod. The camera-tripod system was placed in front of the mechanical analyzer with a distance of about 1 m (Figures S5a,b). The relative position and orientation of the cameras on the left and right were carefully adjusted to get a good field of view that covers all the dots on the model, and then fixed on the slide rail attached to the tripod. The foci of the lenses were adjusted and fixed to be on the model, so that the dots on it were sharply projected onto the image planes of the left and right cameras. The two cameras shot in continuous mode with 5 FPS. All the other camera parameters such as the shutter speed, aperture, ISO, exposure compensation and image quality were set to be identical to minimize timing differences during the continuous shooting mode due to different software and hardware settings. A remote controller (Nikon ML-L3) was used to wirelessly control the left and right camera, so that the continuous shooting of two cameras were triggered simultaneously with the pressing of the shutter button on the controller. The remote shutter control also resulted in minimum image blur by

insulating the vibration when the shutter was triggered by hand. According to a shooting test with 100 frames in 20 s, the maximum difference in the shooting time of the two cameras was ca. 20 ms.

8.3. Individual camera calibration. The main calibration procedure of the left or right camera individually is based on the Camera Calibration Toolbox for MATLAB.^[2] 20 images of a 12×12 checkerboard in different locations were taken with each camera, followed by post-processing of grid corner extraction and calibration optimization. The camera model used in the software package was similar to the model of Heikkilä and Silvén,^[3,4] with the intrinsic parameters consisting of focal length, principal point, skew coefficient and distortions. The radial and tangential distortion model, which is also known as the “Plumb Bob” model, was originated by Brown.^[5,6] Its reduced version was implemented in the software package.^[7] The camera extrinsic parameters were computed during the calibration optimization as well, including the translation vector and the rotation matrix from the checkerboard-fixed frame to the camera frame, which was used in the stereo system calibration step. The calibration optimization is a nonlinear minimization problem based on Maximum Likelihood Estimation.^[7]

8.4. Stereo camera system calibration. The goal in this step is to recover the relative pose of the right camera to the left camera or vice versa, given the relative pose of the calibration checkerboard to each camera from the last calibration step. Let $\{K_i\}$ denote the frame fixed to the calibration checkerboard located in the i th position where two pictures were taken from the left and right camera during the individual camera calibration step. Let $\{A\}$ and $\{B\}$ denote the left and right camera frame, respectively. Given the intrinsic and extrinsic parameters from the previous calibration procedure, we can recover the relative poses of the checkerboard in the i th position with respect to the left and right cameras:

${}^A\mathbf{p}_K^{(i)}, {}^A\mathbf{C}_K^{(i)}, {}^B\mathbf{p}_K^{(i)}, {}^B\mathbf{C}_K^{(i)}$. The relative pose of the right camera with respect to the left camera can then be computed by:

$${}^A\mathbf{p}_B^{(i)} = {}^A\mathbf{p}_K^{(i)} - {}^A\mathbf{C}^{(i)} {}^B\mathbf{C}^{(i)T} {}^B\mathbf{p}_K^{(i)} \quad (\text{S6})$$

$${}^A\mathbf{C}^{(i)} = {}^A\mathbf{C}^{(i)} {}^B\mathbf{C}^{(i)T} \quad (\text{S7})$$

After transforming the rotation matrix ${}^A\mathbf{C}^{(i)}$ into the rotation vector from ${}^A\mathbf{r}^{(i)} \in \mathbb{R}^{3 \times 1}$ with Rodrigues' rotation formula, the relative pose of the two cameras can be estimated by simply taking the element-wise median of the transformation and rotation vectors in different checkerboard locations.

$${}^A\tilde{\mathbf{p}}_B = \text{median}_i {}^A\mathbf{p}_B^{(i)} \quad (\text{S8})$$

$${}^A\tilde{\mathbf{r}} = \text{median}_i {}^A\mathbf{r}^{(i)} \quad (\text{S9})$$

The estimated rotation matrix ${}^A\tilde{\mathbf{C}}$ can then be acquired using the reverse Rodrigues rotation formula.

8.5. Image processing (feature extraction). The simultaneous, continuous shooting of the two cameras began with the compressing of the 3D printed prostate model. On each of the images taken from the model, the feature dots were to be located pixel-wise in the 2D image frame. The 2D image coordinates of the feature dots were computed by finding the pixel with the closest RGB values to a preset reference value in the neighborhood of the initial guess. The Red, Green, and Blue value of the pixel located at indices (x, y) are $R_{(x,y)}, G_{(x,y)}, B_{(x,y)}$, respectively, which are integers ranging from 0 to 255. Let \mathcal{L} denote the neighborhood around the initial guess of the feature location. The estimation of the feature point location (x^*, y^*) is given by:

$$(x^*, y^*) = \underset{x,y \in \mathcal{L}}{\operatorname{argmin}} \left\{ (R_{(x,y)} - R_{ref})^2 + (G_{(x,y)} - G_{ref})^2 + (B_{(x,y)} - B_{ref})^2 \right\} \quad (\text{S10})$$

To eliminate the noise in the image RGB values, the Gaussian blur filter was applied to the neighborhood of the initial guess before solving the minimization problem. The initial guess

and the reference RGB values were manually initialized only for the first image frames from the left and right cameras, simply by picking the feature points by hand in the image and recording its RGB values. The same set of initial parameters were utilized by subsequent image frames and all the computations were performed automatically.

8.6. Post processing (3D trajectory reconstruction). The goal here is to estimate the 3D position of each feature point expressed in the left or right camera frame at every time step, which can be viewed as solving a ray triangulation problem. For simplicity, only the estimation of the 3D trajectory in the left camera frame $\{A\}$ was considered. Given the intrinsic parameters from the individual camera calibration procedure, the 2D pixel projection information was transformed to the 3D unit bearing measurements ${}^A\mathbf{a}_j^{(k)}, {}^B\mathbf{b}_j^{(k)}$, for feature point j on the 3D printed prostate model at the time step k , from the left and right cameras, respectively. To express all bearing measurements from the right camera in the left camera frame, the relative pose estimation ${}^A_B\tilde{\mathbf{C}}$ from step 8.4 was used.

$${}^A\mathbf{b}_j^{(k)} = {}^A_B\tilde{\mathbf{C}} {}^B\mathbf{b}_j^{(k)} \quad (\text{S11})$$

The computations for each time step and for each feature point were identical, and the notation of the bearing measurements in the left camera frame was simplified to

$$\mathbf{v}_1 = {}^A\mathbf{a}_j^{(k)}, \mathbf{v}_2 = {}^A\mathbf{b}_j^{(k)} \quad (\text{S12})$$

Due to the error of the 2D feature extraction on the sampled images in the image processing step, the two projected light rays of the bearing measurements $\mathbf{v}_1, \mathbf{v}_2$ may not intersect at a point, which is the ideal estimation of the feature point location in 3D space. An alternative approach is to find the shortest line segment P_1P_2 that connects the two projected light rays, and estimate the 3D location of the feature point to be the midpoint F of the line segment, as illustrated in Figure S5c. Because $\overrightarrow{{}^AP_1P_2}$ is perpendicular to the bearing vectors $\lambda_1\mathbf{v}_1$ and

$\lambda_2 \mathbf{v}_2$ with scaling factors λ_1 and λ_2 , $\overline{A P_1 P_2} = \lambda_1 \mathbf{v}_1 - \lambda_2 \mathbf{v}_2 - {}^A \tilde{\mathbf{p}}_B$ is in the null space of the 2×2 matrix $[\mathbf{v}_1 \ -\mathbf{v}_2]^T$.

$$\begin{aligned}
 & [\mathbf{v}_1 \ -\mathbf{v}_2]^T (\lambda_1 \mathbf{v}_1 - \lambda_2 \mathbf{v}_2 - {}^A \tilde{\mathbf{p}}_B) = \mathbf{0} \\
 & \Rightarrow [\mathbf{v}_1 \ -\mathbf{v}_2]^T (\lambda_1 \mathbf{v}_1 - \lambda_2 \mathbf{v}_2) = [\mathbf{v}_1 \ -\mathbf{v}_2]^T {}^A \tilde{\mathbf{p}}_B \\
 & \Rightarrow \begin{bmatrix} \|\mathbf{v}_1\|_2^2 & -\mathbf{v}_1^T \mathbf{v}_2 \\ -\mathbf{v}_2^T \mathbf{v}_1 & \|\mathbf{v}_2\|_2^2 \end{bmatrix} \begin{bmatrix} \lambda_1 \\ \lambda_2 \end{bmatrix} = \begin{bmatrix} \mathbf{v}_1^T {}^A \tilde{\mathbf{p}}_B \\ -\mathbf{v}_2^T {}^A \tilde{\mathbf{p}}_B \end{bmatrix} \\
 & \Rightarrow \begin{bmatrix} \lambda_1 \\ \lambda_2 \end{bmatrix} = \begin{bmatrix} \|\mathbf{v}_1\|_2^2 & -\mathbf{v}_1^T \mathbf{v}_2 \\ -\mathbf{v}_2^T \mathbf{v}_1 & \|\mathbf{v}_2\|_2^2 \end{bmatrix}^{-1} \begin{bmatrix} \mathbf{v}_1^T {}^A \tilde{\mathbf{p}}_B \\ -\mathbf{v}_2^T {}^A \tilde{\mathbf{p}}_B \end{bmatrix} \quad (S13)
 \end{aligned}$$

The matrix inversion is valid as long as \mathbf{v}_1 and \mathbf{v}_2 are not parallel to each other. Given the scale factors λ_1, λ_2 , the estimated 3D location of the feature point F in the left camera frame $\{A\}$ can be computed as

$${}^A \tilde{\mathbf{f}} = \frac{1}{2} (\lambda_1 \mathbf{v}_1 + \lambda_2 \mathbf{v}_2 + {}^A \tilde{\mathbf{p}}_B) \quad (S14)$$

Finally, the estimated 3D locations at every time step were connected to form the 3D trajectory of each feature point during the compression test of the 3D printed prostate model.

9. Mapping of the feature dots on the 3D printed prostate model to the corresponding locations on the FEM simulation model

A 3D printed prostate model with feature dots was coated with a thin layer of baby powder (Johnson & Johnson) to increase the scanning quality. A blue light scanner (HDI 109, GoMeasure3D) was used to obtain the 3D geometry and 2D texture mapping. Six scans were carried out every 60° of rotation to obtain a 360° overall scanning. The scanned images were fused together via David 3D laser scanner software (v3.10.4). The scanned digital model and the FEA simulation model were then placed into the CloudCompare software for 3D registration with a universal coordinate system. The location coordinates (x, y, z) of the feature dots on the scanned digital model were used to map the corresponding location with the same coordinates on the FEM simulation model (Figure S6).

10. 3D printing and calibration of the soft tactile sensor

10.1. Fabrication of inks for the soft tactile sensor. The composition of the ionic hydrogel includes 21.48 wt% lithium chloride (Sigma-Aldrich), 7.90 wt% acrylamide monomer (Sigma-Aldrich), 3.16 wt% polyacrylamide (Mw 5,000,000-6,000,000; Sigma-Aldrich), 29.64 wt% Milli-Q ultrapure water (Millipore), 37.60 wt% ethylene glycol (Fisher Chemical), 0.13 wt% N,N'-methylenebisacrylamide crosslinking agent (Sigma-Aldrich), and 0.08 wt% Irgacure 1173 photoinitiator (BASF). The silicone elastomer was prepared by mixing Loctite 5039 Nuva-sil (Henkel) and Semicosil 912 (Wacker) at a ratio of 3:2, and addition of Elastosil CAT UV catalyst (Wacker) at a ratio of 1:10 with respect to the Semicosil 912 base.^[8]

10.2. 3D printing of the soft tactile sensor. A 1 cm × 1 cm sensor device was printed by alternately depositing layers of the two different materials, followed by their photopolymerization via exposure to a UV system (Omnicure S1500, Excelitas Technologies). To facilitate the testing of the devices, copper tape was used as electric contact leads and was inserted into the device during the printing process. Specifically, the first copper lead was inserted after printing the first silicone layer (base) and prior to deposition of the bottom hydrogel electrode, and the second copper contact lead was inserted after printing the top hydrogel electrode and prior to depositing the top silicone encapsulation (cover). In addition, to facilitate the uniform printing of the hydrogel on the hydrophobic surface of the silicone, we treated the underlying silicone surface with 10 wt% solution of benzophenone (Sigma Aldrich) in acetone.

10.3. Calibration of the soft tactile sensor. The 3D printed sensor was calibrated by applying different pressures to the device and measuring the changes in the capacitance. For this purpose, a metal bar was mounted on a vertical axis of a nanopositioning stage (ANT130-L-ZS, Aerotech) to apply cycles of press-release to the device by varying the vertical position of the bar to obtain different values for the applied forces (Figure S9). The applied forces were recorded using a digital scale with a flat surface (Elec3) which was placed underneath the

sensor. The applied pressure values were then calculated by dividing the recorded forces by the sensor area before deformation. In addition, the sensor was connected to a characterization system (B1500A, Agilent Technologies) to observe the changes in device capacitance at each of the press-release cycles. A calibration plot can be obtained for the sensor based on the capacitance changes at each applied pressure. After integration of the sensor onto the 3D printed prostate model, this calibration plot can be used to translate the amount of pressure applied to the model using the surgical tools based on the changes in capacitance of the device.

11. Advanced surgical rehearsal using the 3D printed prostate model

11.1. Endoscopy system for endoscopic view. The endoscopy system consisted of an endoscope (Gyrus ACMI), an LED light source (L9000, Stryker), an endoscopic camera (1288 HD 3-Chip, Stryker), an HD information management system (SDC Ultra, Stryker), a high flow insufflator (40L, Stryker) and an HDTV surgical display (WiSe™, Stryker) (Figure S7). The endoscope was inserted into the urethra of the model and the endoscopic view was observed from the surgical display for the application. The preoperative rehearsal was further carried out under KUB background while placing the 3D printed prostate model between kidney and bladder models for the endoscope application (Figure S8).

11.2. Surgical suturing. Suturing was conducted on the surface of the 3D printed prostate model with the aid of a surgeon and by utilizing a surgical needle for penetration and surgical thread (ETHICON 3-0 PERMA-HAND SILK) for suturing.

11.3. With 3D printed soft tactile sensor for pressure detection. A finger and different diagnostic/surgical tools were applied on the sensor integrated on the surfaces of the 3D printed prostate model (outer surface and urethra inner surface). For each application, three quick press-release and three press-hold-release cycles were applied. The signal responses of capacitance changes of the sensor were then converted into the values of applied pressures via the sensor pre-calibration of capacitance change vs pressure.

Supplementary Information References

- [1] R. W. Ogden, *Proc. R. Soc. A* **1972**, 326, 565.
- [2] J.-Y. Bouguet, Camera calibration toolbox for matlab, **2004**.
- [3] J. Heikkila, O. Silven, presented at *Proc. 13th Int. Conf. Pattern Recogn.*, Vienna, Austria, August, **1996**.
- [4] J. Heikkila, O. Silvén, presented at *IEEE Comp. Soc. Conf. Comp. Vision Pattern Recogn.*, San Juan, Puerto Rico, USA, June, **1997**.
- [5] C. B. Duane, *Photogramm. Eng.* **1971**, 37, 855.
- [6] J. G. Fryer, D. C. Brown, *Photogramm. Eng. Remote Sens.* **1986**, 52, 51.
- [7] Z. Zhang, presented at *Proc. 7th IEEE Int. Conf. Comp. Vision*, Kerkyra, Greece, September, **1999**.
- [8] S. S. Robinson, K. W. O'Brien, H. Zhao, B. N. Peele, C. M. Larson, B. C. Mac Murray, I. M. Van Meerbeek, S. N. Dunham, R. F. Shepherd, *Extreme Mech. Lett.* **2015**, 5, 47.

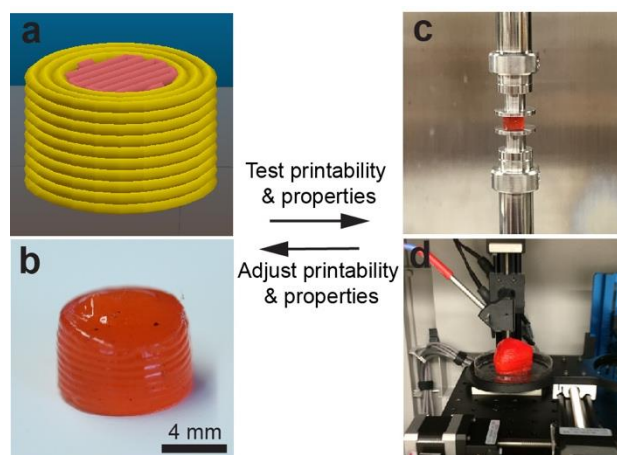


Figure S1. Procedure for adjustment of properties of the customized polymeric inks. a) Sliced STL cylinder model. b) Corresponding 3D printed cylindrical sample using customized polymeric inks. c) Static/dynamic compression tests for the 3D printed cylindrical sample. d) Optical reflection test for the 3D printed prostate model.

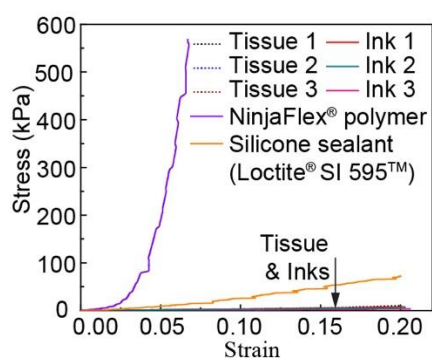


Figure S2. Comparison of mechanical properties via plots of stress vs strain between commercial polymers, tissue, and the customized polymeric inks.

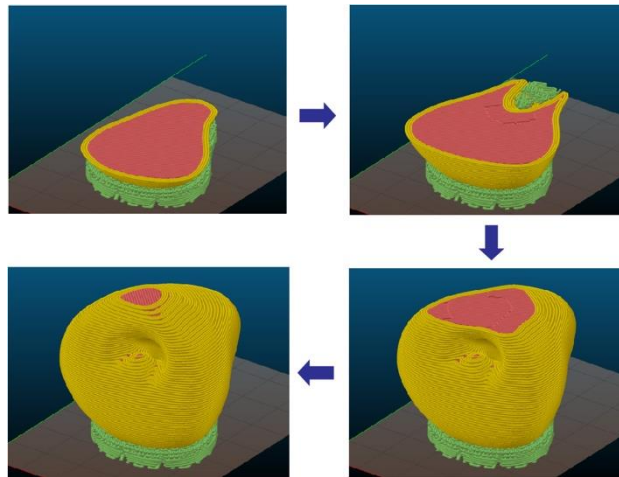


Figure S3. Demonstration of 3D printing steps using sliced STL prostate model.

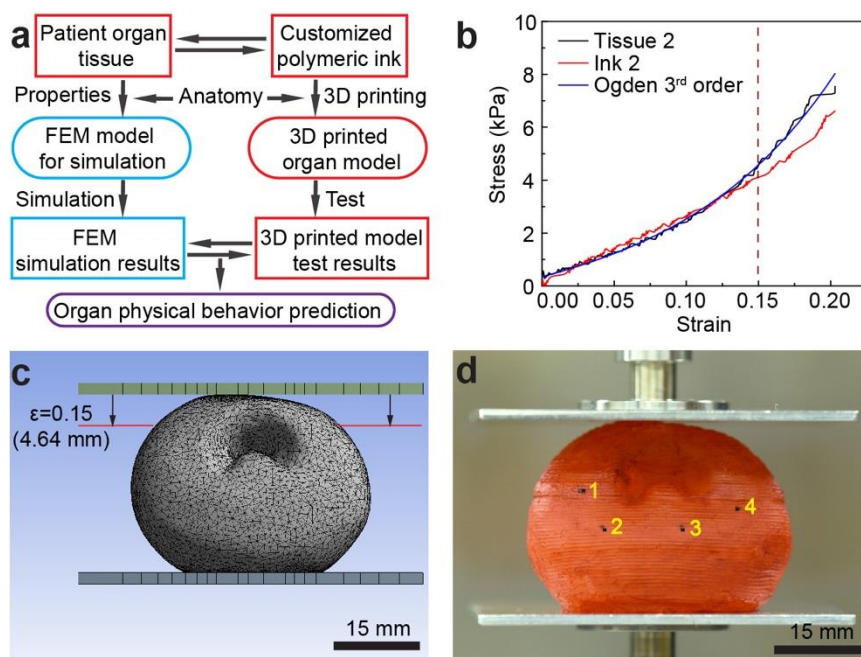


Figure S4. Organ physical behavior via compression of 3D printed organ model and FEM simulation of the same. a) Flow chart for the study of organ physical behavior using the 3D printed prostate model and FEM simulations. b) Stress-strain curves for patient prostate tissue, custom polymeric ink, and Ogden third order model used for FEM simulation. c) Undeformed state of FEM model with patient-specific prostate anatomy and physical properties of tissue. d) 3D printed prostate model with four randomly selected feature dots in their original positions before model compression.



Figure S5. Customized stereo system and tracking mechanism. a,b) Schematic (a) and picture (b) of the stereo system setup using dual cameras for tracking the displacement of different regions on the model. c) Schematic of ray triangulation for the tracking mechanism.

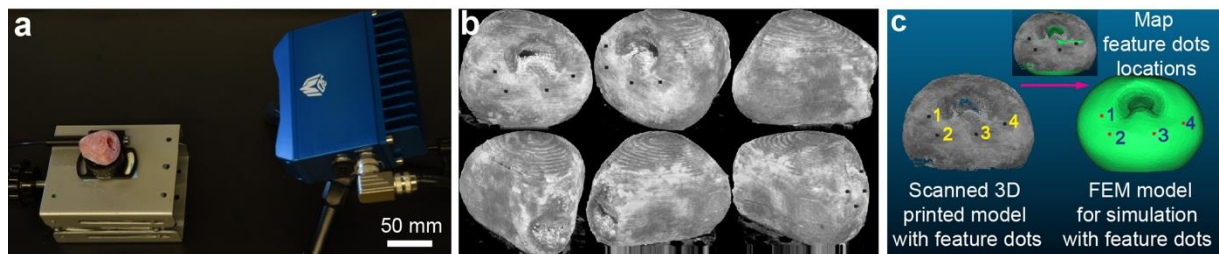


Figure S6. Scanning of the 3D printed prostate model for mapping feature dots. a) Scan system setup for the 3D printed prostate model with feature dots. b) Scanned images of 3D printed prostate model with feature dots information. c) Mapping of the feature dots on the 3D printed prostate model into the corresponding locations on the FEM model for simulation.

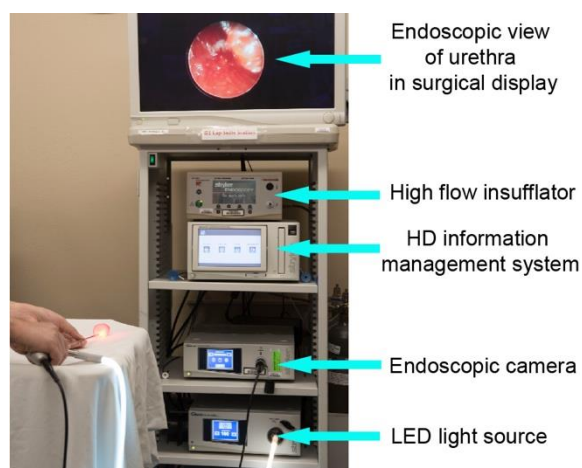


Figure S7. Overview of setup of the endoscope tower station and 3D printed prostate model as an example of its use in surgical rehearsal.

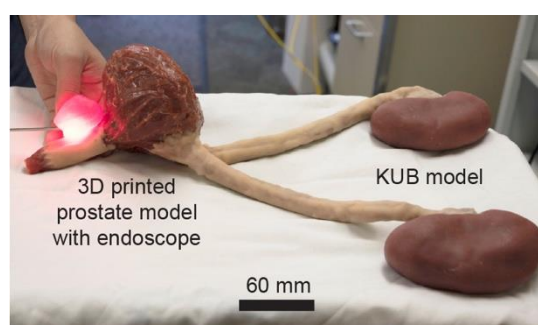


Figure S8. Surgical rehearsal involving applying an endoscope in the urethra of the 3D printed prostate embedded in a CREST KUB model.

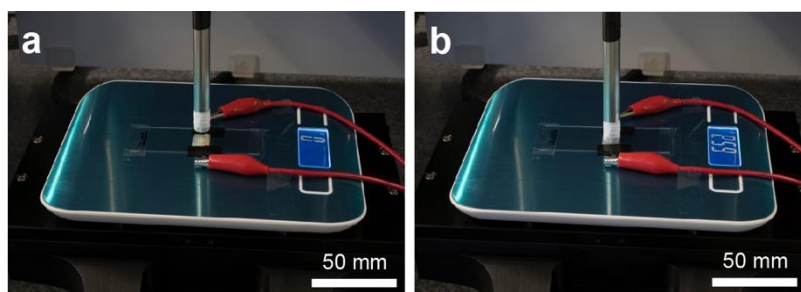


Figure S9. Calibration of the 3D printed soft tactile sensor. a,b) Characterization of the 3D printed soft tactile sensor before pin compression (a) and under pin compression (b) on a digital balance.

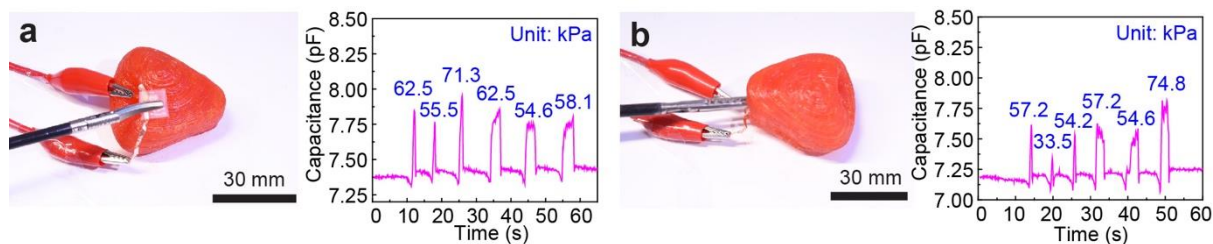


Figure S10. Two quantitative surgical rehearsal applications using the 3D printed prostate model. a) Quantitative surgical aid application of the 3D printed prostate model for applying surgical scissors on the sensor integrated on the outer surface of the model and the corresponding pressure responses from the capacitance changes of the sensor. b) Quantitative surgical aid application of the 3D printed prostate model for applying a surgical grasper on the sensor integrated on the urethra surface inside of the model, and the corresponding pressure responses from the capacitance changes of the sensor.

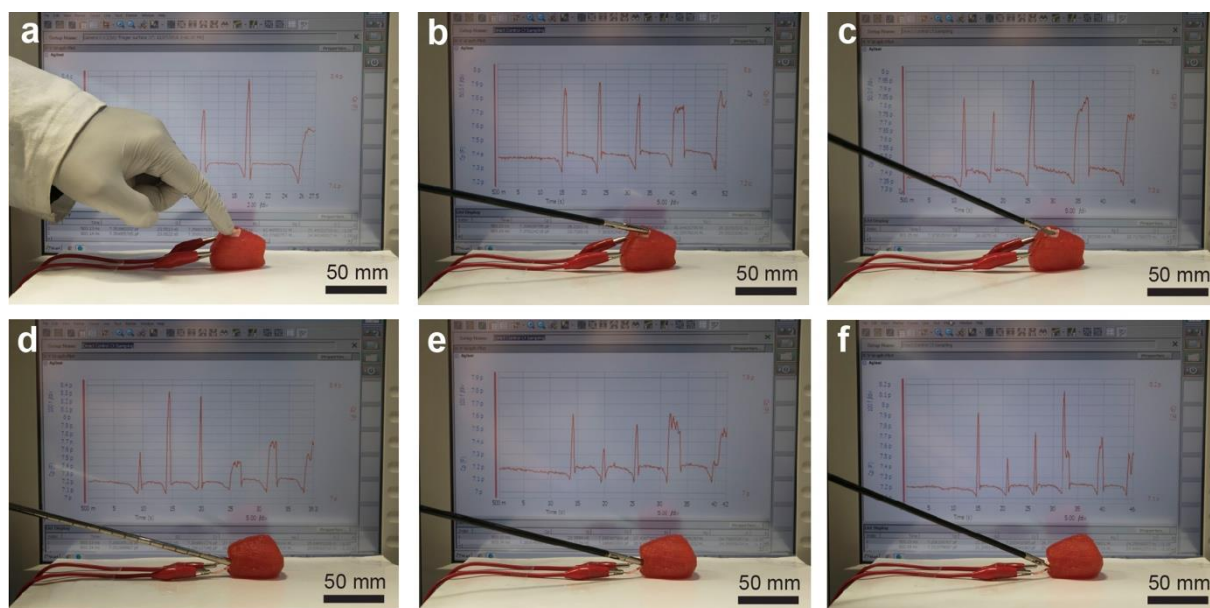


Figure S11. Real-time surgical rehearsal on the model outer surface and urethra inner surface of the 3D printed prostate model with responses of the integrated 3D printed tactile sensor. a-c), Real-time surgical rehearsal by applying finger (a), surgical grasper (b) and surgical scissors (c) on the sensor integrated on the outer surface of the 3D printed prostate model with the corresponding response signal from the sensor recorded in terms of changes in capacitance. d-f) Real-time surgical rehearsal by applying endoscope (d), surgical grasper (e) and surgical scissors (f) on the sensor integrated on the urethra surface inside of the 3D printed prostate model with the corresponding signal from the sensor recorded in terms of changes in capacitance.

Table S1. Formulations for the customized polymeric inks to fit tissue mechanical properties.

(w/w/w)	Active agent	Bulking agent	Additives (Coloring)	Young's modulus (kPa)
Ink 1	0.95	3.05	0.002	30.5 ± 3.8
Ink 2	0.90	3.10	0.002	25.7 ± 3.2
Ink 3	0.82	3.18	0.002	10.3 ± 3.0

Note: The properties of the inks with the given formulations might vary slightly from batch to batch. For accurate properties, test and adjustment of prepared inks before printing is recommended.

Table S2. Parameters of the Ogden third order model for the FEM simulation.

	α_1	α_2	α_3	μ_1	μ_2	μ_3
Tissue 2	12.84	13.00	12.84	33.20	11.44	490.74

Movie Captions

Movie S1. MRI of patient prostate. The movie does not contain protected health information.

Movie S2. 3D printing process ($\times 20$ speed) for prostate model using the customized inks and patient prostate anatomy.

Movie S3. MRI of the 3D printed prostate model.

Movie S4. FEM simulation of total deformation for compression of patient prostate.

Movie S5. Compression test for the 3D printed prostate model with feature dots.

Movie S6. Endoscopic view of urethra surface from the 3D printed prostate model.

Movie S7. Surgical suturing on the 3D printed prostate model.

Movie S8. Finger press on the tactile sensor integrated on the outer surface of the 3D printed prostate model.

Movie S9. Surgical grasper press on the tactile sensor integrated on the outer surface of the 3D printed prostate model.

Movie S10. Surgical scissors press on the tactile sensor integrated on the outer surface of the 3D printed prostate model.

Movie S11. Endoscope press on the tactile sensor integrated on the urethra surface of the 3D printed prostate model.

Movie S12. Surgical grasper press on the tactile sensor integrated on the urethra surface of the 3D printed prostate model.

Movie S13. Surgical scissors press on the tactile sensor integrated on the urethra surface of the 3D printed prostate model.